Materials Characterization 207 (2024) 113433

Contents lists available at ScienceDirect

Materials Characterization

journal homepage: www.elsevier.com/locate/matchar

Sigma phase kinetics in DSS filler metals: A comparison of sigma phase formation in the as-welded microstructure of super duplex stainless steel and hyper duplex stainless steel

Andres Acuna [a,b], Kaue Correa Riffel [b], Antonio Ramirez [b,*]

[a] Lincoln Electric, Cleveland, OH, USA
[b] Ohio State University - Department of Materials Science and Engineering, Columbus, OH, USA

ARTICLE INFO

Keywords:
Phase transformation
Precipitation
Duplex stainless steel
Intermetallic
Nucleation
Diffusion-controlled growth
Avrami's exponent

ABSTRACT

This study investigates and compares the kinetics of sigma phase formation in established Super Duplex Stainless Steel (SDSS) and recently developed Hyper Duplex Stainless Steel (HDSS) filler metal wires. Experimental sigma phase time-temperature-transformation (TTT) maps were developed, revealing nearly equivalent interface area/volume, resulting in similar sigma phase kinetics for 1% volume despite the higher Cr and Mo content in HDSS. However, the growth rate to 5% and 10% sigma phase volumes was slightly higher in HDSS. The sigma phase kinetics in both SDSS and HDSS were analyzed using the exponential Johnson-Mehl-Avrami-Kolmogorov (JMAK) approach based on experimental TTT data. Linearized plots from the JMAK calculations showed a transition in kinetics mechanism from eutectoid decomposition and interface-controlled growth to a diffusion-controlled growth stage in both materials. The higher volumes and morphologies of the sigma phase were found to be diffusion-dependent, mainly occurring during the second kinetics stage. The influence of HDSS's higher Cr and Mo content on the growth rate was observed for these higher volumes. For applications within the 1% sigma phase limit, both wires exhibited equivalent susceptibility to sigma phase formation, regardless of the higher alloying in HDSS.

1. Introduction

Duplex Stainless Steels (DSS) are extensively utilized in various industries for their outstanding corrosion resistance, combined with good toughness and yield strength, attributed to a balanced microstructure containing 50% ferrite and 50% austenite. The pitting resistance equivalent number (PREn = %Cr + 3.3% (Mo + 0.5%W) + 16 %N in wt %) is employed to classify the materials based on their localized corrosion resistance, considering the composition [1–3].

Among DSS materials, the Super Duplex Stainless Steel (SDSS) has gained prominence, boasting a PREn between 40 and 48. Additionally, the recently developed Hyper Duplex Stainless Steel (HDSS) exceeds a PREn 48 incorporating Cr, Mo, and N. While these alloying elements enhance corrosion performance, they can also lead to the stabilization of undesired phases. Notably, DSS materials are susceptible to intermetallic precipitation, such as Sigma and Chi phases, when exposed to temperatures ranging from 600 °C to 1100 °C. Among these, the sigma phase is the predominant precipitate in highly alloyed DSS. It nucleates at the interfaces between austenite and ferrite and grain edges. Once formed, the sigma phase grows into the ferrite phase, consuming Cr and Mo, thereby reducing corrosion resistance [4,5] and hindering mechanical properties [5–7].

Extensive research has been conducted on sigma phase formation and its effects on SDSS base metal over the past three decades [8–13]. In contrast, limited investigations have been reported on HDSS sigma phase kinetics [14–17]. Moreover, most intermetallic formation studies have focused on base metals and heat-affected zones, with minimal attention given to the sigma phase kinetics of weld and filler metal wires. Filler metals typically possess higher alloying content than base metals, and they are extensively used in various applications, such as cladding,

Abbreviations: TTT, Time-Temperature-Transformation; JMAK, Johnson-Mehl-Avrami-Kolmogorov; PREn, Pitting resistance equivalent number; DSS, Duplex stainless steel; SDSS, Super duplex stainless steel (40<PREn>48); HDSS, Hyper duplex stainless steel (PREn>48); α, Ferrite phase; γ, Austenite phase; γ_2, Secondary austenite phase; σ, Sigma phase; SEM, Scanning Electron microscopy; EBSD, Electron backscattered diffraction.

* Corresponding author.
E-mail address: ramirez.49@osu.edu (A. Ramirez).

https://doi.org/10.1016/j.matchar.2023.113433
Received 4 September 2023; Received in revised form 23 October 2023; Accepted 24 October 2023
Available online 27 October 2023

welding of thick sections, repairs, and additive manufacturing, resulting in a substantial amount of weld metal. In such applications, complex thermal histories involving multiple re-melting and solidification cycles can promote sigma phase formation. Hence, comprehensive research is essential to develop tools for comprehending, characterizing, modeling, and avoiding the formation of the sigma phase in filler metals, thus enhancing the overall understanding of DSS materials.

The main difference in microstructure formation arises from the alloy's chemical composition. The higher Cr and Mo content in HDSS is not the primary factor but rather the N content and its impact on the ferrite matrix phase. High N content in HDSS promotes increased austenite formation and alters the partitioning coefficients of Cr and Mo [18]. Zhang et al. [16] demonstrated the influence of N on precipitation behavior in HDSS, showing that higher nitrogen content leads to reduced differences in Cr and Mo content between austenite and ferrite phases. Moreover, increasing N content has been found to lower the sigma phase nucleation force.

Thermodynamic calculations indicate that SDSS exhibits a typical fully ferritic solidification characteristic of DSS. In contrast, the high levels of austenite stabilizers, including Ni and N, in HDSS ensure austenite formation at the end of solidification [19]. This composition hinders ferrite volume and grain size, resulting in a higher austenite volume. Additionally, the sigma solvus temperature is elevated in HDSS, which influences the chemical composition of ferrite at that temperature. The higher concentrations of Cr, Mo, and N in the austenite phase of HDSS are evident through thermodynamic and PREn calculations.

The Johnson-Mehl-Avrami-Kolmogorov - JMAK kinetics describes the nucleation and growth phase transformation process [20] and has been successfully applied to sigma phase formation in DSS [21–23] being expressed as:

$$f = 1 - e^{(-kt^n)} \tag{1}$$

Where f is the transformed sigma volume fraction ($0 < f < 1$), t is the transformation time, and n is the Avrami's exponent, indicating the order of the solid-state reactions. The coefficient k is related to the energy barrier for the sigma phase formation and is described as an Arrhenius equation as follows [20,22,24]:

$$k = k_0\, e^{\left(-\frac{Q_\sigma}{RT}\right)} \tag{2}$$

Where k_0 is a pre-exponential constant, Q_σ is the empirical activation energy for sigma phase formation, it aggregates all processes occurring, T is the temperature in Kelvin, and R is the gas constant. Both n and k can be obtained graphically from the linearized form of the equation, $ln(-ln(1-f)) = n(ln(t)) + ln(k)$, by calculating n from the fitted inclination of the transformation data and determining k from the vertical intercept.

Acuna and Ramirez [25–27] established a sigma phase kinetics formation analysis on solubilized HDSS wires. However, sigma phase kinetics forming in the as-welded weld metal microstructure was still not analyzed.

In this study, an in-depth sigma phase kinetics analysis in the most corrosion-resistant DSS materials, the SDSS and the HDSS is presented. Simultaneously analyzing both filler metals with the same thermal histories enables a direct kinetics comparison and gives a behavior perspective of the recently developed HDSS with reference to the well-established SDSS filler metal ER2594.

2. Materials and methods

2.1. Materials

Fig. 1 presents the source and configuration of both materials. The as-welded precipitation bars specimens (70 mm × 10 mm × 5 mm) were machined from a three-layered cladded mockup, Fig. 1 (c). The specimens were machined from different locations, avoiding the start and end

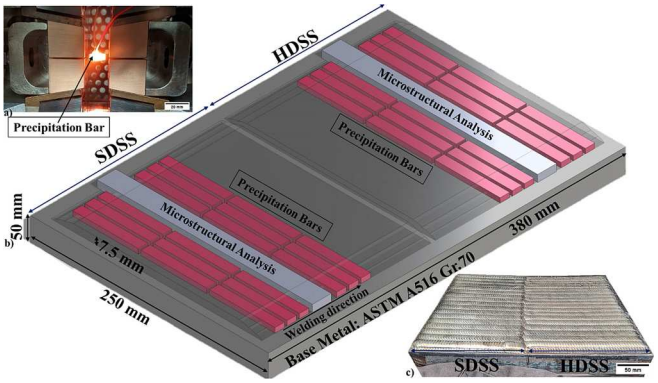

Fig. 1. Materials specimen. (a) specimen precipitation experiment on the Gleeble. (b) CAD schematic of specimen location of the precipitation bars in red and microstructural analysis specimen in gray. (c) cladded mockup from which the "as-welded" specimens were machined. (For interpretation of the references to colour in this figure legend, the reader is referred to the web version of this article.)

regions of the welding beads, as shown in Fig. 1 (b). To ensure consistency, the cladded mockup used the same heating input (1.65 kJ/mm – 200 A, 14 V 100 mm/min, 15 l/min 98%Ar + 2% O_2), interpass temperature (200 °C), and wire diameter (1.2 mm). Table S2 in the supplementary material provides the welding parameters used). Therefore, the only change is the filler metal chemical composition from SDSS to HDSS.

Table 1 presents wire chemical composition measured through Optical Emission Spectroscopy (OES). Due to the fact that the nitrogen emission line is in extremely short wavelengths region for OES, its amount was also validated using a combustion spectrometer Leco TC600.

2.2. Experimental procedure

The experimental design used a Gleeble 3800 physical simulator to construct a precipitation map. In this equipment, the machined precipitation bars with as-welded microstructure were heated at 100 °C/s until reaching a specific isothermal aging temperature (a table of the heat treatment conditions can be found in the supplementary material). The sample was then held at this temperature for a defined aging time and subsequently cooled at a minimum rate of 37 °C/s [25].

Microstructural characterization provided the intermetallic volumetric fractions for each sample, and these measurements were combined with time and temperature data to develop the experimental kinetics time-temperature-transformation (TTT) contour plot maps. The data was interpolated using the Kriging [28] method, and the resulting isovolumetric lines represented the interpolated kinetic TTT curves.

Intermetallic volume fractions were quantified using quantitative electron microscopy (FEI Apreo LoVac High Resolution). Sample preparation involved grinding from 240 to 1200 grit, followed by 1 μm diamond paste polishing, and a final 0.02 μm colloidal silica polishing for three hours. Microstructural etching was performed using a modified version of Ramirez et al. [29] dual-step electrolityc etching process. This process involved a 40% HNO_3 + 60% distilled water solution for interphase etching, with a first step of 1.3 V for 20 s, followed by 0.9 V for 60–240 s for preferential ferrite etching.

The procedure for quantifying phase fractions by digital image analysis, thresholding gray scale images from SEM is described in detail in previous works [25,26]. The JMAK kinetic law was used to model the sigma phase kinetics formation. In this analytical method, the experimental precipitation data was taken in 25 °C steps from 775 °C to 1000 °C. The data from the Eq. 1 generated linearized (ln(−ln(1-f)) x ln (t)) plots that graphically described sigma phase formation. From the

Table 1
OES Measured chemical composition in wt% from the filler metal wires.

Material	Fe	C	Cr	Ni	Mo	N	Co	Mn	PREn
HDSS 27.7.5.L	Bal.	0.023	26.05	6.31	4.74	0.40	1.32	0.96	48.0
SDSS ER2594	Bal.	0.01	25.05	9.25	3.90	0.27	0.05	0.42	42.2

linearized plots, the Avrami's exponent and n and time activation k were calculated.

3. Results and discussion

3.1. Material and microstructure characterization

Both materials received equivalent thermal histories from the same heat input and interpass temperatures, welding parameters are presented in the supplementary material. As such, the SDSS and the HDSS microstructures were similar, according to Fig. 2 (a) and (b). The SDSS phase distribution presented 56.6% ±3.0% ferrite volume, while the HDSS formed 52.9% ±1.5% ferrite. The difference in ferrite content is due to the higher nitrogen in the HDSS alloy promoting faster austenite stabilization. Fig. 2 (c) and (d) present low magnification EBSD IPF maps revealing that the microstructures sawn in Fig. 2 (a) and (b) are equivalent and, therefore representative of the whole microstructure.

SEM EBSD analysis provided complementary information on the microstructure grain size and interface length/volume between ferrite and austenite. Table 2 presents microstructural data from EBSD measurements at higher magnification from Fig. 2 on the as-welded specimen.

The measurements present a similar order of grain size in both materials, marked by the statistically equivalent average grain size. Ferrite measurements were challenging because the solidified microstructure presented a large ferritic matrix with austenite grains embedded inside, hence the wider standard error on the ferrite grains.

In addition, calculations of the interfacial length per unit of volume using the EBSD data indicated the SDSS (0.016 μm^{-2}) corresponding to 91% of the HDSS (0.018 μm^{-2}). Therefore, both materials present

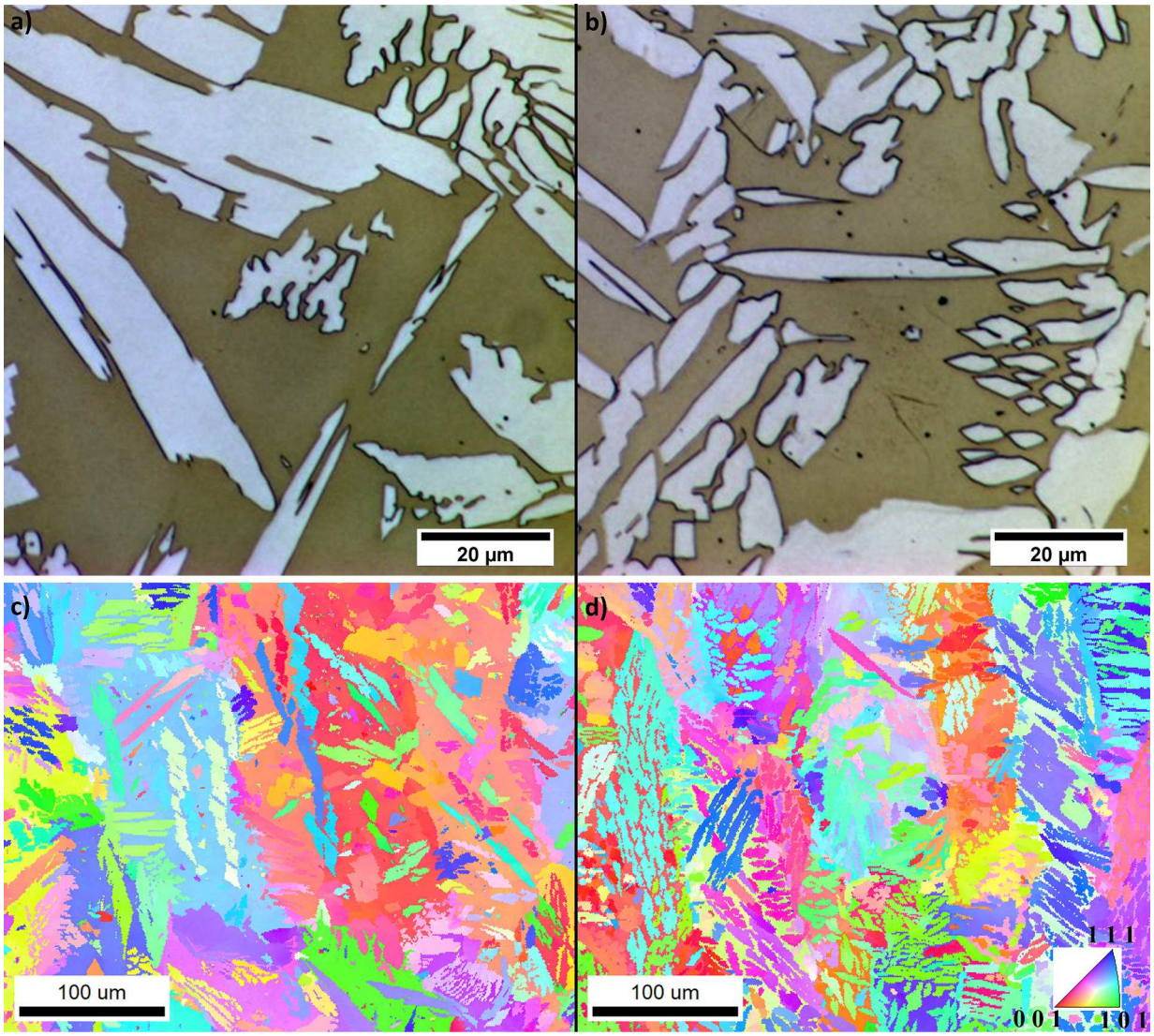

Fig. 2. As-welded microstructure. Optical image with high magnification (a) SDSS and (b) HDSS. Low magnification EBSD IPF map of (c) SDSS and (d) HDSS, showing repeatability of the microstructures shown in (a) and (b).

Table 2
EBSD measured grain size of SDSS and HDSS in the as-welded condition.

	Both phases		Austenite		Ferrite		
	Average [μm^2]	Std. E.* ±[μm^2]	Average [μm^2]	Std. E.* ±[μm^2]	Average [μm^2]	Std. E.* ±[μm^2]	Interface length/volume [μm^{-2}]
SDSS	151.8	71.0	179.1	66.9	76.8	109.0	0.016
HDSS	115.4	58.9	96.21	31.5	124.8	114.0	0.018

* Note: The standard error (Std. E.) is calculated for a confidence interval of 95%.

phases in the same order of magnitude, statistically equivalent, and equivalent interfacial length per unit of volume.

3.2. Microstructural characterization and kinetics

The quantitative metallography performed for the isothermal precipitation experiment samples yielding data (time, temperature, and sigma phase volume fraction) extrapolated to create sigma phase experimental interpolated contour maps [25,26], according to Fig. 3. Tables with as-welded sigma phase volume quantification are provided as supplementary material, Table S3 for the SDSS and Table S4 for the HDSS. Fig. 3 is the graphical visualization, through data interpolation, of experimental precipitation results, in other words, experimental sigma phase kinetics. These charts represent the precipitation data as sigma phase experimental TTT maps of the SDSS and HDSS weld metal.

Due to the similar starting microstructure and similar chemical composition, the kinetics behavior of SDSS and HDDS contour plots also presents affinities according to Fig. 3. In particular to 1% of sigma volume, which represents the initial stages of phase transformation. In the SDSS weld metal, the maximum kinetics occurs at 900 °C until 300 s. After this time, the maximum kinetics temperature decreases with time increase. Conversely, the as-welded HDSS precipitation temperature range is more comprehensive than the SDSS until 300 s, and the maximum kinetics temperature at 875 °C does not change within the tested time range. It is believed that while the SDSS might have reached exhaustion of the nucleation sites and reduced Cr diffusion due to the sigma phase growth, the HDSS with higher interface length per unit of volume and higher Cr has not shown nucleation sites saturation within the 800 s tested.

The similar kinetics in Fig. 3 is also seen in the microstructure evolution in Fig. 4, presenting a sigma phase formed through divorced precipitation at a temperature higher than the maximum kinetics temperature and ferrite decomposition into cellular nucleation of $\sigma + \gamma_2$. Duly and Brechet [30] studied nucleation mechanisms considering discontinuous precipitation nodules in Mg—Al alloys. Double seam nodules, *i.e.,* growing on both sides of a grain boundary, are typical of the Tu-Turnbull [31–33] mechanism. Conversely, nodules at a single side of a grain boundary are typical of the Fournelle-Clark [34] nucleation mechanism. His observation indicated that in the low-temperature domain, the nucleation mechanism proposed by Tu-Turnbull [31–33] dominates while occurring concomitantly with the Fournelle-Clark [34] nucleation mechanism. As the temperature increases, the proportion of single seam nodules, the Fournelle-Clark mechanism, also increases.

If the temperature is sufficiently high, where the allotriomorphs are incapable of pinning, the boundary movement and discontinuous precipitation become virtually impossible, and general nucleation occurs [30].

Fig. 4 illustrates sigma phase evolution at temperatures above, near, and below the maximum kinetics temperature, at various tested times and temperatures. SDSS is depicted in the left column, figures (a – d), while HDSS is shown in the right column, figures (e – f).

Fig. 4 (a) shows the initial sigma phase formation at 950 °C for 100 s (in correlation with the graph in Fig. 3 a), forming 1.07 ± 0.51 volume. Small nuclei form on grains' triple corners while earlier nucleated grains consume the ferrite matrix, creating sigma phase grains longer than 15 μm.

In Fig. 4 (b): Large colony denoted by white dashed contour on the left, with large plates on the right. Both cellular colony nucleation mechanisms Tu-Turnbull's [33] and Fournelle – Clark's [34] are active at temperatures below the maximum kinetics, with a dominance of Tu-Turnbull's mechanism, according to Duly et al. [30] Fig. 4 (c): Same dominant sigma phase morphology at 765 °C for 500 s. Longer time promotes sigma phase and secondary austenite lamella growth, with prior reaching 7.02% ±1.06% volume. At 950 °C for 600 s, Fig. 4 (d), the sigma phase plates are larger, growing to 6.92% ±2.04% volume.

As mentioned before, the formed microstructure is also somewhat similar in HDSS because of the similar chemical composition and kinetics. However, chromium nitride presence is more often seen in the

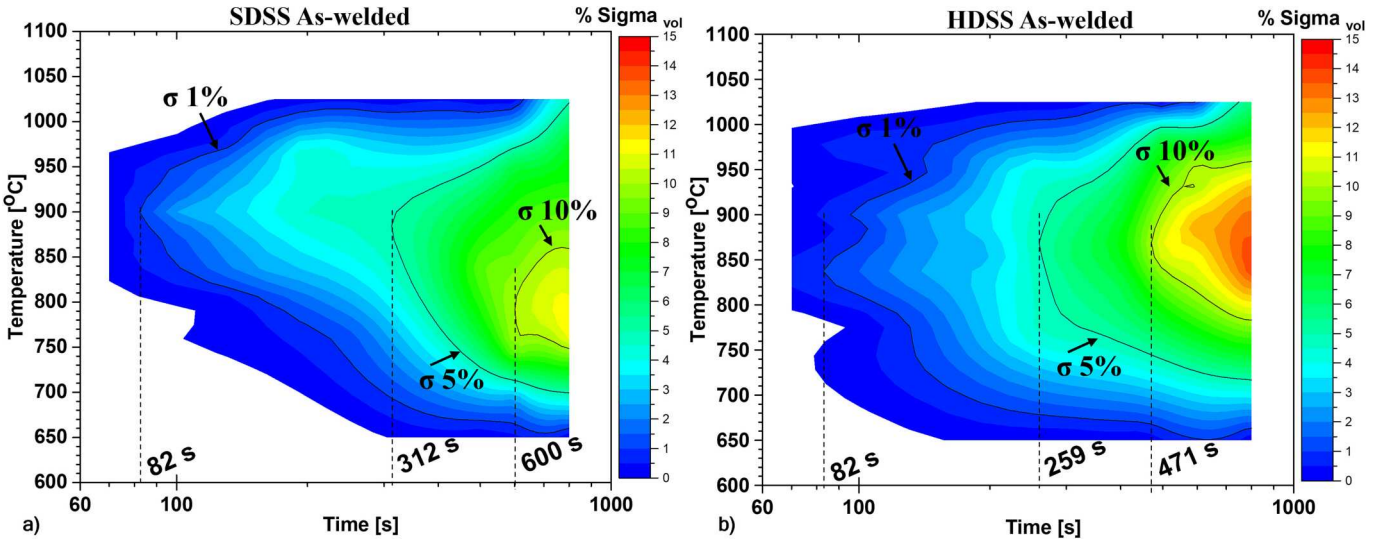

Fig. 3. As-welded microstructure sigma phase experimental TTT map comparison. SDSS material (a) and HDSS material (b).

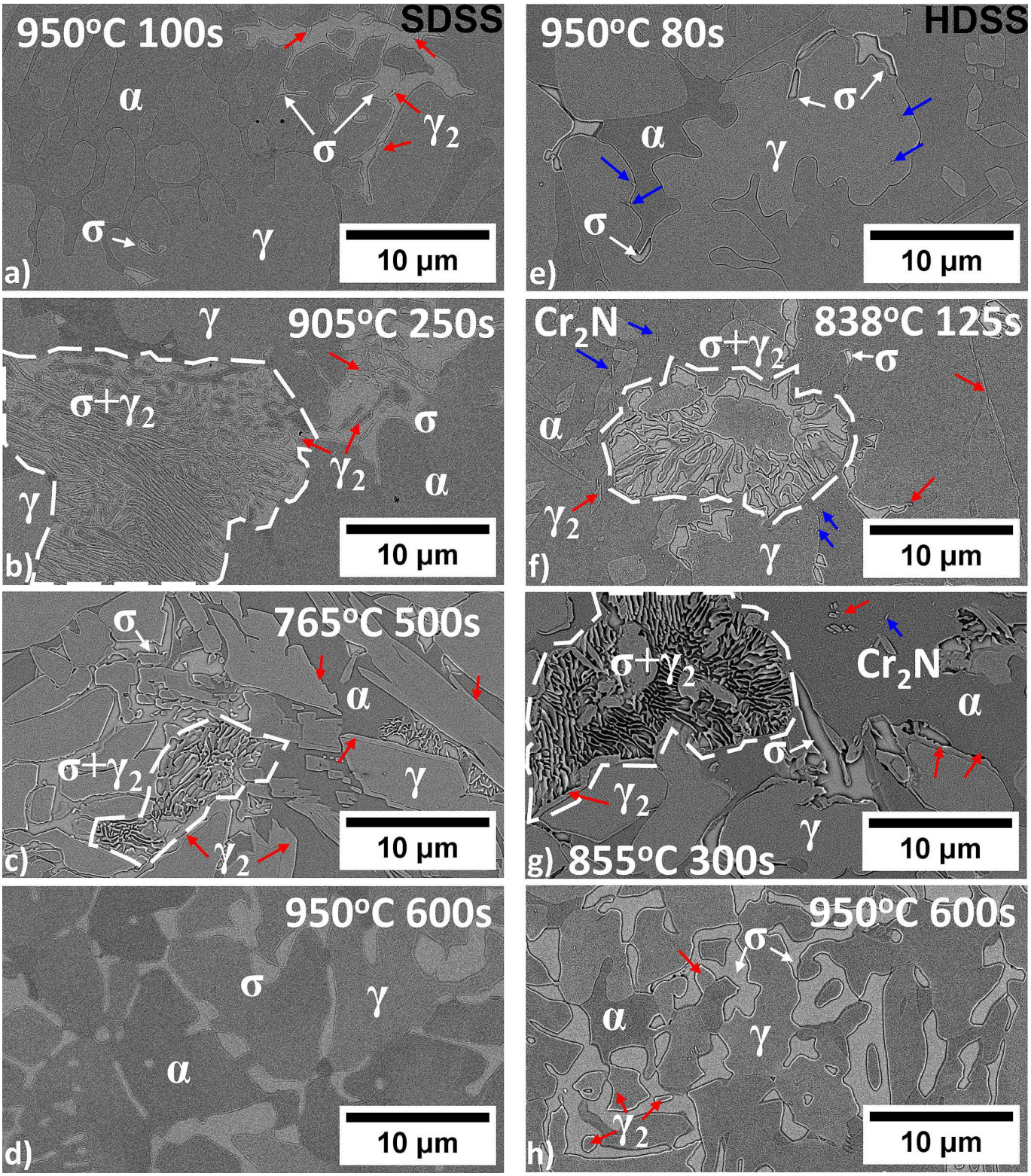

Fig. 4. Sigma phase evolution as a function of isotherm heat treatment (in Gleeble) on the SDSS on the left column (a – d) and HDSS on the right column (e – h). White arrows mark the sigma phase presence, red arrows mark the secondary austenite presence, blue arrows mark the Cr_2N presence, and the white dashed lines indicate the $\sigma + \gamma_2$ colonies. SEM secondary electron detector. (For interpretation of the references to colour in this figure legend, the reader is referred to the web version of this article.)

HDSS, which is richer than the SDSS in nitrogen and chromium. In Fig. 4 (e), at 950 °C for 80 s, the nucleation is starting, as only 0.25% ±0.15% of the sigma phase is found. Therefore, no secondary austenite was seen as the Cr and Mo depletion on the ferrite matrix might not yet be significant to cause austenite stabilization at these early stages of transformation. Chromium nitrides, indicated by the blue arrows, are present at α/γ interfaces or trapped within an austenite grain at the former interface before the grain growth.

Fig. 4 (f), morphologies from both types of nucleation are also seen. Chromium nitrides, blue arrows, are also present at the γ/α interfaces and intragranular. Besides the secondary austenite formed from ferrite decomposition, $\alpha \rightarrow \sigma + \gamma_2$, intergranular secondary austenite is formed at the γ/α associated with Cr_2N precipitates. These nitrides remain trapped in the austenite grain as the new γ_2/α advances [29,35,36]. In addition, intragranular secondary austenite is also formed within the ferrite matrix nucleated at the intragranular chromium nitrides. Both forms of secondary austenite found agreed with the mechanism proposed by Ramirez et al. [29,35] and should follow the preferential $(111)_\gamma||(110)_\alpha||(0001)_{Cr2N}$ orientation relationship.

In Fig. 4 (g), increasing the time to 300 s at 855 °C, 6.01% ±0.77% volume of sigma phase is formed. The white dashed area indicates a lamellar σ + γ2 colony starting from an austenite grain and consuming the ferrite matrix until the colony growing front impinges another austenite grain. Secondary austenite is along the previous γ/α interfaces and intragranular assisted by Cr_2N precipitates.Transformation at 600 s is shown in Fig. 4 (h) at 950 °C mainly presents the sigma phase and secondary austenite growth with a small presence of Cr_2N. The nitride reduced due to dissolution at high temperature for the treatment time.

Fig. 5 depicts a large colony formed in 500 s at 765 °C on the SDSS. Within the image center, a σ + γ2 lamellar colony emerges from an austenite sheave grain, indicated by the purple arrows. The colony expands, consuming the ferrite matrix and covering an area of 240 μm^2. As the colony expands, the growth direction of the lamellas changes, as denoted by the green dashed lines. At the top of the image, plates of sigma phase grains formed through divorced precipitation are also observed. However, the dominant structure is the lamellar one. The orange arrows mark the new formed interfaces, including γ/γ_2, α/γ_2, and σ/γ_2.

Secondary austenite growing as an extension of the primary austenite observed at lower temperatures but not at high temperatures. The red arrows indicate the presence of secondary austenite, which can occur in both morphologies: as an extension of the preceding austenite and in association with the precipitated sigma phase. Small chromium nitride precipitates at the interface of the secondary austenite are marked with a blue arrow.

Fig. 6 depicts an SEM backscattered electron image revealing the microstructure of an HDSS sample heated at 855 °C for 300 s. The cellular morphology of the sigma phase suggests the simultaneous occurrence of Fournelle's and Turnbull's nucleation mechanisms, leading to the formation of the sigma phase and secondary austenite lamellas. While both mechanisms are observed at 855 °C, the dominant mechanism is Fournelle and Clark, prominently visible in the image center, denoted by the white dashed lines. Additionally, Cr_2N precipitation is observed within the ferrite matrix [29] and at the γ/α interfaces, marked by the blue arrows. This Cr_2N precipitation aids in the nucleation and growth of secondary austenite within the ferrite matrix, indicated by the red arrows. The formation of γ_2 introduces new interfaces, including γ/γ_2, α/γ_2, and σ/γ_2, as highlighted by the yellow arrows. Consequently, a higher occurrence of secondary austenite is observed at lower temperatures.

3.3. Kinetics calculations

The Johnson-Mehl-Avrami-Kolmogorov (JMAK) kinetic equation [21–23,37,38] is a tool commonly used to describe phase transformation kinetics. In this study, the kinetics calculations utilize experimental TTT map data for both materials. Fig. 7 presents two linearized plots, $\ln(-\ln(1-f))$ as a function of $\ln(t)$, for each material at temperatures of 775 °C, 900 °C and 975 °C, which are below, close and above the maximum kinetics temperature.

Both materials exhibit a dual kinetics behavior, *i.e.*, indicating a transition in the sigma phase kinetics mechanism. The data is divided into two linear stages: the first stage, in blue markers characterized by a higher Avrami's exponent (n), and the second stage, in orange markers displaying a lower n value.

Christian [20] describes that within the discontinuous precipitation and interface-controlled growth(n *between 1 and 4*), different values of n might describe distinct formation conditions. In this case, $n = 2$ indicates "grain edge nucleation after saturation," and $n = 1$ suggests "grain boundary nucleation after saturation".

The slope change and the values calculated for n suggest that both materials have a first kinetic mechanism characteristic of discontinuous precipitation, eutectoid reactions, and interface-controlled growth. This is followed by a diffusion-controlled growth secondary kinetic mechanism. The change of slope occurred with different volumetric fractions as the temperature changed. The SDSS presented the slope change after transformations of 7.5% vol. at 775 °C (a), 4.5% vol. at 900 °C (c), and 3.7% vol. at 975 °C (e) while the HDSS presented the transition at 250 s and 4.3%vol. at 775 °C (b) and at 900 °C (d), only changing the transition time at 975 °C (f) but with the same 4.3% sigma phase volume.

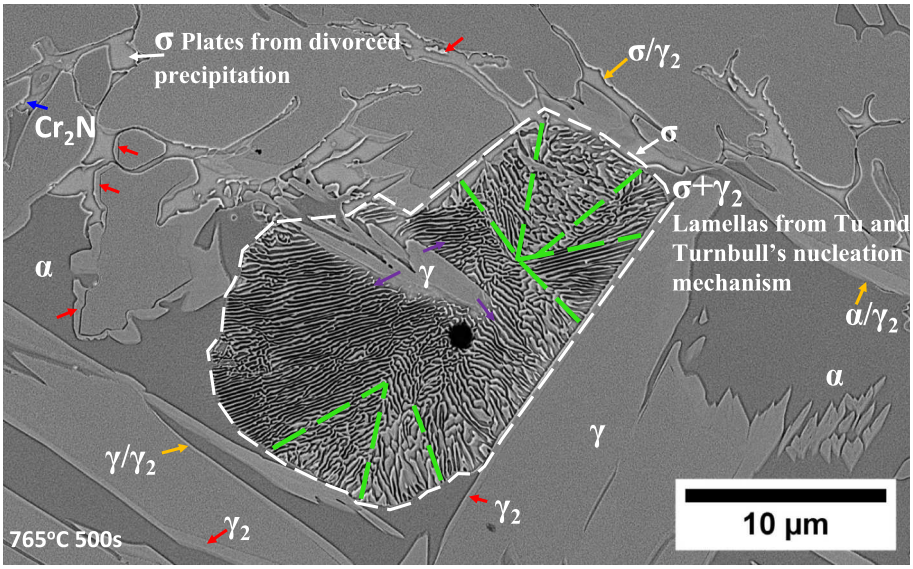

Fig. 5. SDSS high magnification detail of a sizeable cellular colony formed in 500 s at 765 °C. The white arrows are sigma phase grains, red arrows mark the secondary austenite, the blue arrow indicates Cr_2N presence, the yellow arrows indicate the new α/γ_2 formed interface, and the purple arrows indicate the radial direction of the lamellas growth from an α/γ interface. The dashed green lines mark the lamella's growth direction change.

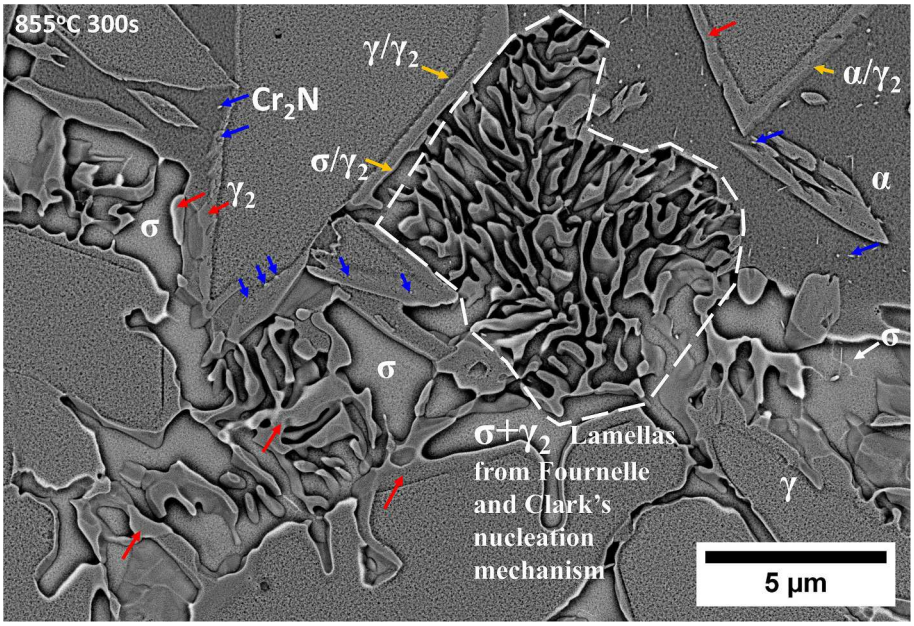

Fig. 6. HDSS high magnification detail of the microstructure formed in 300 s at 855 °C, a cellular colony is highlighted with dashed lines. The white arrows are sigma phase grains, red arrows mark the secondary austenite, the blue arrows indicate Cr_2N presence intragranular and at the interfaces, and the yellow arrows indicate the newly formed interface (σ/γ_2, γ/γ_2, and α/γ_2).

Although some inflection changes emerge at very short times, *e.g.*, 900 °C curves, the *n* and *k* calculated at these points do not match the experimental phase transformation data. However, the inflections at extended times yield closer results to experimental data.

This shift in the kinetics mechanism is consistent with previous findings reported in the literature [13,20,39–41]. Studies by Elmer et al. [39], Dos Santos et al. [40], and Da Fonseca et al. [13] have identified the occurrence of double kinetics as the initial stage of discontinuous precipitation or interface-controlled growth, followed by a second stage of diffusion-driven growth in both duplex and super duplex stainless steels. Marques et al. [41] have noted that the first kinetic stage is heavily influenced by the presence of the Chi phase, which serves as a nucleation site for the sigma phase. In contrast, the second stage involves the diffusion growth of the sigma phase into the ferrite matrix.

Table 3 displays the Avrami's exponent (*n*) as a function of temperature in the first and second slopes. The SDSS material exhibits a higher average *n* value of 2.38 compared to the HDSS value of 1.91. This indicates that the SDSS undergoes a faster transformation rate at a given temperature, resulting in a steeper inclination in the phase transformation sigmoidal curve.

It is commonly observed that *n* remains relatively independent of temperature in most transformations, while *k* shows significant variation markedly [20]. In this study, the analyzed precipitation temperature range for both materials shows considerable variation in *n*. However, near the nose of the curve, at the maximum kinetics, the Avrami's exponent *n* displays low variability, irrespective of the predominant kinetics mechanism.

Therefore, this research used the average Avrami's *n* exponent and calculated *k* at 25 °C increments from the experimental precipitation data. This approach results in a single Avrami-type equation for each slope of the sigma phase transformation, where *n* is a constant number and *k* is an array of values as a function of the temperature. Within the precipitation temperature range, at temperatures in between the calculated *k* values, interpolation can be used to obtain *k* at a specific temperature.

Outlined by the diffusion-controlled growth, on the second slope, the Avrami's exponent values are smaller. The SDSS varies between 0.17 and 1.38 and the HDSS is between 0.71 and 1.19. This values range, within the diffusional growth kinetics mechanism, suggests the thickening of needles or plates [20]. The values obtained in this research are a great match with other authors in various other Duplex Stainless Steel families [39–41].

The kinetics results directly connect with the microstructure, as the cellular structures formed below the maximum kinetics temperature were not frequently observed during the initial kinetics mechanism. Instead, they became more predominant during the second kinetics mechanism, which involves diffusional growth, as previously shown in Fig. 4.

Duly and Brechet [30] classified the discontinuous precipitation based on its nucleation mechanism, namely Tu and Turnbull and Fournelle and Clark. The term "nucleation" here refers to the cell or colony ($\sigma + \gamma 2$) nucleation, not the individual precipitates.

It has been demonstrated that the kinetics of this reaction depends on the overall growth rate of the cell [20,42]. Therefore, the kinetics results from this study suggest that both cell formation and the sigma phase within the cell are influenced by diffusional growth. This is consistent with the expected lamellar colony formation, where diffusion of Cr and Mo from the ferritic matrix occurs, leading to the formation of the sigma phase, while the Cr and Mo-depleted region transforms into austenite simultaneously.

From the calculated coefficients, a single JMAK equation is obtained to describe the transformed sigma phase volume as a function of time for each temperature for each kinetics mechanism, as summarized in Table 4.

In this approach, the Avrami's exponent *n* is considered constant to all temperatures, and *k* is temperature dependent array listed in Table 3, k_{SD1} and k_{SD2} for the SDSS alloy and k_{HD1} and k_{HD2} HDSS alloy.

Validation of the JMAK kinetics can be obtained by calculating the TTT curves using Table 4 equations. Fig. 8 presents the sigma phase JMAK calculated TTT curves of 1%, 5%, and 10% volume fractions overlapped with the sigma phase experimental precipitation maps.

In Fig. 8, the JMAK calculated TTT properly captured the transformation on the SDSS although the biggest divergence found occurred at the maximum kinetics temperature range (a). This difference is understood on the *k* temperature dependence as 900 °C was the maximum value and in the *k* distribution inflection point, combined with the *n*

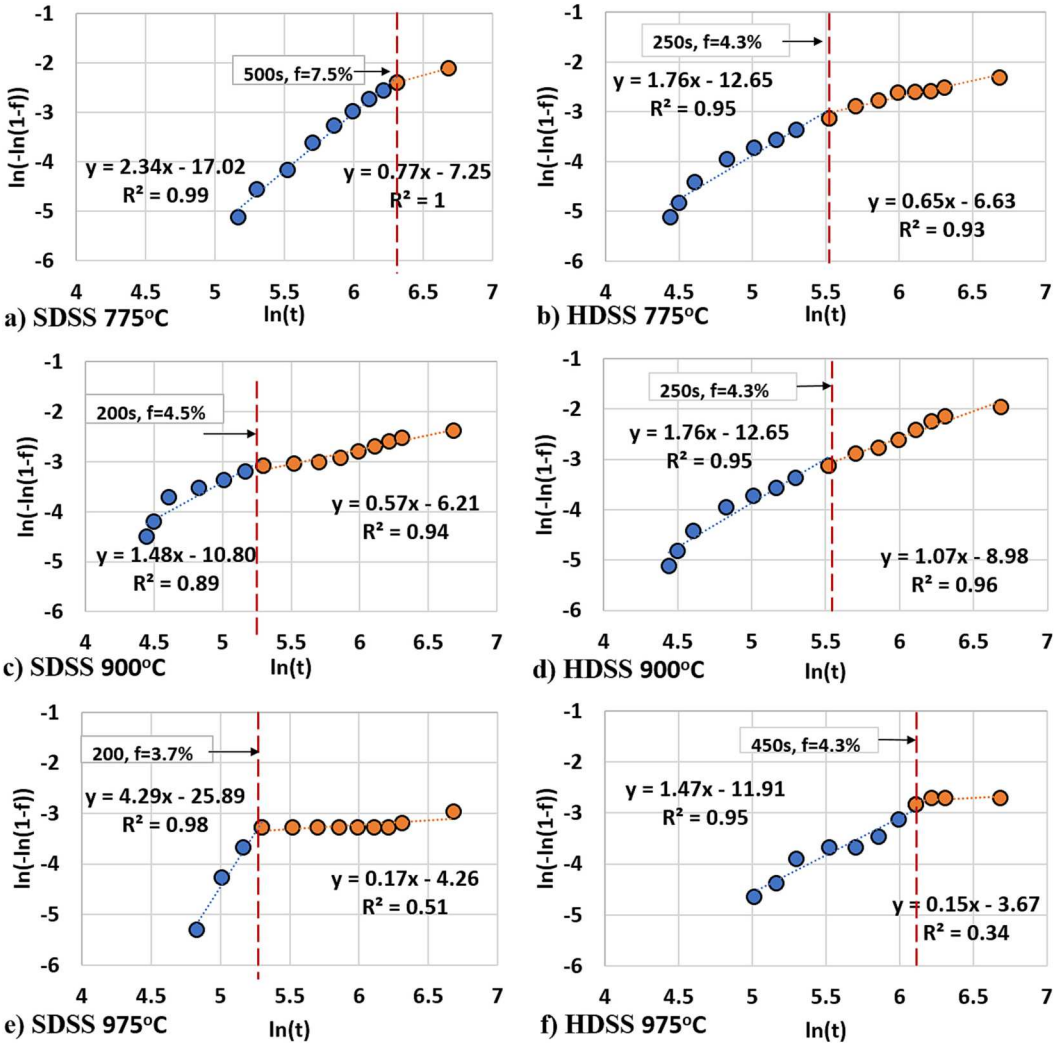

Fig. 7. As-welded microstructure JMAK linearized plots. SDSS (a, c, and e) and HDSS (b, e, and f) at 775 °C, 900 °C, and 975 °C. The red dashed line marks the change of kinetics mechanism, with the arrow indicating the time and formed volume fraction until the transition. (For interpretation of the references to colour in this figure legend, the reader is referred to the web version of this article.)

Table 3
SDSS and HDSS JMAK Avrami's exponent n and coefficient k calculated from the experimental data. Values are presented for the first slope (discontinuous precipitation or interface-controlled growth), and second slope (diffusion-controlled growth).

	SDSS				HDSS			
	1st slope		2nd slope		1st slope		2nd slope	
Temperature	n	k_{SD1}	n	k_{SD2}	n	k_{HD1}	n	k_{HD2}
675	1.55	1.38E-13	1.38	1.57E-03	2.11	1.48E-07	0.40	1.57E-03
700	1.93	1.84E-07	1.17	1.64E-02	2.31	1.05E-07	0.12	1.64E-02
725	2.61	4.92E-09	0.25	1.33E-02	2.18	3.20E-07	0.24	1.33E-02
750	2.57	8.15E-09	0.69	5.42E-03	1.96	1.07E-06	0.46	5.42E-03
775	2.34	4.05E-08	0.77	1.76E-03	1.76	3.21E-06	0.61	1.76E-03
800	1.98	4.18E-07	0.66	9.33E-04	1.58	7.98E-06	0.71	9.33E-04
825	1.97	8.60E-07	1.16	9.80E-05	1.49	1.36E-05	1.10	9.80E-05
850	1.98	1.12E-06	0.93	1.91E-04	1.55	9.80E-06	1.01	1.91E-04
875	1.90	1.94E-06	0.74	1.91E-04	1.56	9.76E-06	1.01	1.91E-04
900	1.48	2.03E-05	0.57	1.26E-04	1.76	3.21E-06	1.07	1.26E-04
925	1.88	2.28E-06	0.56	1.23E-04	1.94	9.38E-07	1.06	1.23E-04
950	2.30	2.34E-07	0.43	1.11E-04	2.88	3.55E-07	1.05	1.11E-04
975	4.29	5.71E-12	0.17	6.57E-05	1.99	4.55E-07	1.08	6.57E-05
1000	4.53	7.64E-13	0.24	1.76E-05	1.73	8.27E-07	1.19	1.76E-05
Average	**2.38**	1.96E-06	**0.69**	3.31E-03	**1.91**	3.70E-06	**0.79**	2.88E-03
Min	**1.48**	1.38E-13	**0.17**	1.51E-02	**1.49**	1.05E-07	**0.71**	1.76E-05
Max	**4.53**	2.03E-05	**1.38**	2.55E-06	**2.88**	1.36E-05	**1.19**	1.64E-02

Table 4
Sigma phase JMAK equations of first and second kinetics mechanism for the SDSS and HDSS in the solubilized and as-welded microstructures.

Alloy	Kinetics mechanism	Discontinuous precipitation or interface-controlled growth	Diffusional growth
SDSS	As-welded	$f = 1 - e^{(-k_{SD1}t^{2.38})}$	$f = 1 - e^{(-k_{SD2}t^{0.69})}$
HDSS	As-welded	$f = 1 - e^{(-k_{HD1}t^{1.91})}$	$f = 1 - e^{(-k_{HD2}t^{0.79})}$

fitted parameter. Comparatively, the HDSS JMAK based on the experimental data (b) also shows less divergence at the maximum kinetics temperature where k presented a maxima. Nevertheless, the experimental-based JMAK calculation presented a fair agreement for the 1% sigma phase for both materials (58 s on the SDSS and 29.7 s on the HDSS), according to Table 5.

In contrast, the JMAK calculations of higher volumes, 5% and 10%, did not match the experimental. The offset from Table 5 reaches 532.8 s on the SDSS and 284.4 on the HDSS. At the higher volumes nucleation and diffusional growth occurs simultaneously, requiring coupled calculation on both kinetics mechanisms. With further phase transformation the nucleation sites becomes exhausted and gradually diffusional growth becomes dominant. The overprediction suggest that, at this higher volume, the diffusional-growth rate is slower than precipitation.

4. Conclusions

This work presented the kinetics of the sigma phase in SDSS and HDSS filler metals. Both materials were assessed and compared using experimental precipitation and JMAK analytical calculations based on experimental precipitation TTT data. The described kinetics offered valuable insights into the susceptibility of sigma phase formation in HDSS wires, with a comparison perspective to widely used SDSS wires. Based on the obtained results, the following conclusions can be drawn:

1. Sigma phase kinetics on HDSS is equivalent to SDSS up to 1% volume.
2. The HDSS higher Cr and Mo play a bigger role in the sigma phase growth, as a slightly faster growth rate was found to form 5% and 10% volume.
3. The sigma morphologies were compatible with the ferrite decomposition ($\alpha \rightarrow \sigma + \gamma 2$), presenting sigma and secondary austenite. However, the discontinuous "lamellar" morphology was mainly seen in the diffusion-controlled stage.
4. Sigma phase formation in the SDSS and HDSS filler metals presented a double kinetics dominant mechanism. The first kinetics mechanism is mainly nucleation driven from the eutectoid precipitation, but it also includes initial interface-controlled growth. In contrast, the second kinetics mechanism is diffusion-driven and comprises the coarsening of the established grains.
5. JMAK analysis described the sigma phase transformation with a single equation for each kinetics mechanism, precipitation, and growth for each material and microstructure considered. Each equation had a constant n and an array of k as a function of temperature.

Declaration of generative AI and AI-assisted technologies in the writing process

During the preparation of this work the author(s) used ChatGPT 3.5 and Grammarly in order to readproof, enhance grammar, and reading flow. After using this tool/service, the author(s) reviewed and edited the content as needed and take(s) full responsibility for the content of the publication.

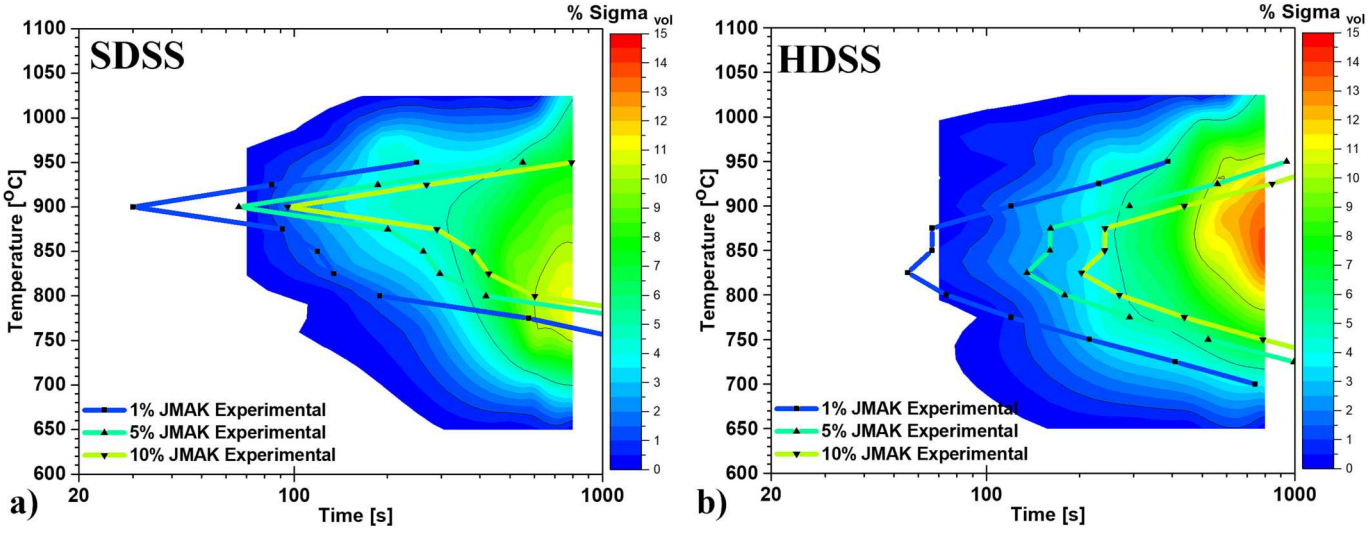

Fig. 8. JMAK calculated sigma phase TTT curves of volumes 1%, 5%, and 10% overlapped with the sigma phase experimental TTT map. The SDSS material is presented in (a) and the HDSS material in (b) as-welded microstructure.

Table 5
Sigma phase maximum kinetics TTT data of 1%, 5%, and 10% volume.

Data	Wire	1% vol time [s]	Temperature [°C]	5% time vol [s]	Temperature [°C]	10% vol time [s]	Temperature [°C]
Experimental	SDSS	82	887–913	312.5	876–890	600.3	778–805
	HDSS	82.2	830–845	259.1	858–875	470.9	859–875
JMAK	SDSS	24	900	48	900	67.5	900
	HDSS	52.5	825	125	825	186.5	825

Declaration of Competing Interest

The authors declare the following financial interests/personal relationships which may be considered as potential competing interests.

Andres Acuna reports financial support was provided by Manufacturing and Materials Joining Innovation Center.

Data availability

The raw/processed data required to reproduce these findings cannot be shared at this time as the data also forms part of an ongoing study.

Acknowledgments

The authors thank the Manufacturing and Materials Join-ing Innovation Center (Ma2JIC) and NSF (IUCRC program,awards 1539992, 1822144, and 2052747). OSU Center forElectron Microscopy and Analysis (CEMAS) for its supportin microscopy. Industry mentors R. Menon, M. Denault, P.Björnstedt, and V. Hosseini for providing the material and fruitful technical discussions. N. Daubenmier for the support for Python coding, and Dr. Eric Brizes for the support and reference on the kinetics approach.

Appendix A. Supplementary data

Supplementary data to this article can be found online at https://doi.org/10.1016/j.matchar.2023.113433.

References

[1] M. Knyazeva, M. Pohl, Metallograph. Microstruct. Analy. 2 (2013) 343–351.
[2] M. Knyazeva, M. Pohl, Metallograph. Microstruct. Analy. 2 (2013) 113–121.
[3] API, API Publishing Services, 1220 L Street, NW, Washington, DC 20005, 2016, p. 38.
[4] J.O. Nilsson, Mater. Sci. Technol. 8 (1992) 685–700.
[5] E.O. Hall, S.H. Algie, J. Inst. Met. 94 (1966) 61.
[6] J.O. Nilsson, P. Kangas, T. Karlsson, A. Wilson, Metall. Mater. Trans. A-Phys. Metallur. Mater. Sci. 31 (2000) 35–45.
[7] C.-C. Hsieh, ISRN Metall. 2012 (2012) 1–16.
[8] I.J. Marques, F.J. Silva, T.F.A. Santos, J. Alloys Compd. (2020) 820.
[9] E.M. Cojocaru, D. Raducanu, A. Nocivin, V.D. Cojocaru, J. Adv. Res. 30 (2021) 53–61.
[10] A.G.C. dos Santos, N.F. Ignacio, M.S. Fernandes, D.M. Baia, F.N. Moreira, W.L. D. Assis, P.R. Rios, J. Mater. Res. Technol.-Jmr&T 15 (2021) 2625–2632.
[11] A.S. Fedorov, A.I. Zhitenev, D.A. Strekalovskaya, A.A. Kur, A.A. Alkhimenko, Metals (2021) 11.
[12] G.S. da Fonseca, P.S.N. Mendes, A.C.M. Silva, Metals (2019) 9.
[13] G.S. da Fonseca, P.M. de Oliveira, M.G. Diniz, D.V. Bubnoff, J.A. de Castro, Mater. Res.-Ibero-American J. Mater. 20 (2017) 249–255.
[14] B.B. Zhang, Z.H. Jiang, H.B. Li, S.C. Zhang, H. Feng, H. Li, Mater. Charact. 129 (2017) 31–39.
[15] D.H. Kim, N.H. Kim, H.W. Lee, Mater. Sci. Technol. 36 (2020) 783–792.
[16] B.B. Zhang, H.B. Li, S.C. Zhang, Z.H. Jiang, Y. Lin, H. Feng, H.C. Zhu, Mater. Charact. (2021) 175.
[17] J. Wang, W.L. Chen, H.J. Meng, Y.S. Cui, C.L. Zhang, P.D. Han, J. Iron Steel Res. Int. 26 (2019) 452–461.
[18] B. Josefsson, J.-O. Nillson, A. Wilson, in: J. Charles (Ed.), Duplex Stainless Steels '91, Les Édition de Physique, Les Ulis, France, 1991, pp. 67–78.
[19] G. Chai, P. Kangas, 21st European Conference on Fracture, (Ecf21) 2, 2016, pp. 1755–1762.
[20] J.W. Christian, The Theory of Transformations in Metals and Alloys, Pergamon, Amsterdam ; Boston, 2002.
[21] W.A. Johnson, R.F. Mehl, Trans. American Instit. Minin.aMetallurg. Engineers 135 (1939) 416–442.
[22] M. Avrami, J. Chem. Phys. 7 (1939) 1103–1112.
[23] M. Avrami, J. Chem. Phys. 9 (1941) 177–184.
[24] H.S. Ray, S. Ray, Kinetics of Metallurgical Processes, Springer, 2018.
[25] A. Acuna, A.J. Ramirez, Mater. Charact. (2023) 200.
[26] A. Acuna, A. Ramirez, R. Menon, P.-Å. Björnstedt, L. Carvalho, ASME 2021 Pressure Vessels & Piping Conference, 2021.
[27] A. Acuna, A. Ramirez, K.C. Riffel, Science and Technology of Welding and Joining, 2023, pp. 1–9.
[28] M.L. Stein, Interpolation of Spatial Data: Some Theory for Kriging, Springer Science & Business Media, 1999.
[29] A.J. Ramirez, J.C. Lippold, S.D. Brandi, Metall. Mater. Trans. A-Phys. Metallur. Mater. Sci. 34A (2003) 1575–1597.
[30] D. Duly, Y. Brechet, Acta Metall. Mater. 42 (1994) 3035–3043.
[31] K.N. Tu, D. Turnbull, Acta Metall. 15 (1967) 369.
[32] K.N. Tu, D. Turnbull, Acta Metall. 15 (1967) 1317.
[33] K.N. Tu, D. Turnbull, Acta Metall. 17 (1969) 1263.
[34] R.A. Fournelle, J.B. Clark, Metall. Trans. A. 3 (1972), 2757-2767-2767.
[35] A.J. Ramirez, S.D. Brandi, J.C. Lippold, Sci. Technol. Weld. Join. 9 (2004) 301–313.
[36] A.J. Ramirez, Escola Politécnica, University of São Paulo, São Paulo, 2001.
[37] M. Avrami, J. Chem. Phys. 2 (1940) 212.
[38] A. Kolmogorov, Isvestiia Academii Nauk SSSR - Seriia Matematicheskaia 1, 1937, pp. 333–359.
[39] J.W. Elmer, T.A. Palmer, E.D. Specht, Metall. Mater. Trans. A-Phys. Metallur. Mater. Sci. 38A (2007) 464–475.
[40] D.C. Dos Santos, R. Magnabosco, Metall. Mater. Trans. A-Phys. Metallur. Mater. Sci. 47A (2016) 1554–1565.
[41] I.J. Marques, A.D.A. Vicente, J.A.S. Tenorio, T.F.D. Santos, Mater. Res.-Ibero-American J. Mater. 20 (2017) 152–158.
[42] I. Machado, Escola Politécnica, Universidade de São Paulo, São Paulo, 1999.